PHOTONICS Research

Topological edge states in a photonic Floquet insulator with unpaired Dirac cones

HUA ZHONG,[1] YAROSLAV V. KARTASHOV,[2] YONGDONG LI,[1] MING LI,[3] AND YIQI ZHANG[1,*]

[1] *Key Laboratory for Physical Electronics and Devices, Ministry of Education, School of Electronic Science and Engineering, Xi'an Jiaotong University, Xi'an 710049, China*
[2] *Institute of Spectroscopy, Russian Academy of Sciences, Moscow 108840, Russia*
[3] *State Key Laboratory of Transient Optics and Photonics, Xi'an Institute of Optics and Precision Mechanics of Chinese Academy of Sciences, Xi'an 710119, China*
**Corresponding author: zhangyiqi@xjtu.edu.cn*

Received 29 March 2024; revised 21 June 2024; accepted 3 July 2024; posted 5 July 2024 (Doc. ID 524824); published 6 September 2024

Topological insulators are most frequently constructed using lattices with specific degeneracies in their linear spectra, such as Dirac points. For a broad class of lattices, such as honeycomb ones, these points and associated Dirac cones generally appear in non-equivalent pairs. Simultaneous breakup of the time-reversal and inversion symmetry in systems based on such lattices may result in the formation of the unpaired Dirac cones in bulk spectrum, but the existence of topologically protected edge states in such structures remains an open problem. Here a photonic Floquet insulator on a honeycomb lattice with unpaired Dirac cones in its spectrum is introduced that can support unidirectional edge states appearing at the edge between two regions with opposite sublattice detuning. Topological properties of this system are characterized by the nonzero valley Chern number. Remarkably, edge states in this system can circumvent sharp corners without inter-valley scattering even though there is no total forbidden gap in the spectrum. Our results reveal unusual interplay between two different physical mechanisms of creation of topological edge states based on simultaneous breakup of different symmetries of the system. © 2024 Chinese Laser Press

https://doi.org/10.1364/PRJ.524824

1. INTRODUCTION

Dirac points are specific degeneracies, where two bands touch each other, representative for linear spectra of many periodic systems, including honeycomb, triangular, Kagome, and Lieb lattices. A dispersion relation is linear around Dirac points, which leads to unusual dispersion dynamics of the wavepackets exciting these points [1]. A variety of physical effects associated with the presence of Dirac points are reported in material sciences, acoustics, optics, and physics of matter waves. In particular, honeycomb lattices with Dirac degeneracies [2–5], representing photonic analogues of graphene [6], are widely used for construction of topological insulators—novel materials, where excitations can propagate along the edges of the structure, but not in its bulk [7–10]. In usual honeycomb lattices Dirac points emerge in six corners of the Brillouin zone, in pairs corresponding to non-equivalent $\mathbf{K}$ and $\mathbf{K}'$ points. However, in Ref. [11] a system with "parity anomaly" was suggested, which may possess unpaired Dirac cones if the time-reversal symmetry and the inversion symmetry of the system are broken simultaneously. The existence of the unpaired Dirac cones implies that massless chiral fermions in such a system lose anomaly cancelling partners with opposite chirality, and thus their appearance breaks the "fermion doubling" theorem [11]. However, due to the unique nature of the unpaired Dirac points and specific symmetry properties that the system possessing them should manifest, the search of such materials is a challenging and open problem.

Different approaches can be used to break time-reversal symmetry in photonic or optoelectronic systems. Among them is the utilization of gyromagnetic optical materials in external magnetic fields [12], or polariton condensates with pronounced spin-orbit coupling in magnetic fields [13–15]; see also Ref. [8]. This effect can also be achieved by using longitudinal modulations in waveguide-based systems, such as photonic Floquet insulators on helical waveguide arrays [16], where a number of topological phenomena have been predicted and observed in linear and nonlinear regimes [17–20]. In these latter systems the breakup of time-reversal symmetry is achieved due to the effective gauge field arising from waveguide modulations [21–23]. By the way, the Floquet waveguide arrays always provide promising results in light manipulations [24–26]. Unpaired Dirac points can, in principle, be observed in helical square waveguide arrays, as suggested in Refs. [27,28], where introduction of the difference into phases of helical waveguide rotation in two sublattices also breaks inversion symmetry of the structure [29–31]. Experimentally, unpaired Dirac points were observed for microwaves in gyromagnetic materials [32], while transitions between regimes with broken inversion and time-reversal symmetries in gyromagnetic structures were reported in Ref. [33]. Very recently, unpaired Dirac points were also proposed and observed in a photonic crystal consisting of Y-shaped gyromagnetic rods [34]. Nevertheless, unpaired Dirac points remain elusive at optical frequencies in waveguiding systems. Topological edge states, which should have unique properties in such materials connected with unusual structure of their linear spectra lacking total gaps, have never been reported, to the best of our knowledge.

In this work, we show that such topological edge states can be observed when one simultaneously introduces into a honeycomb waveguide array the helicity of waveguides, resulting in breakup of its time-reversal symmetry, and also the detuning between its two sublattices, resulting in breakup of the inversion symmetry of the structure. Notice that the approach utilizing sublattice detuning [35–41] is also quite involved in the investigations of the valley Hall effect [42] where, however, the system possesses the total gap, in contrast to the system with unpaired Dirac points considered here. We show that the bulk spectrum of our system has a unique structure with gaps opened between three $\mathbf{K}'$ points and preserved Dirac cones at three $\mathbf{K}$ points. Remarkably, we find that the domain wall between two arrays with different signs of sublattice detuning supports topologically protected edge states, which, in complete contrast to valley Hall systems, feature asymmetric projected dependence of a quasi-propagation constant on Bloch momentum and connect two different bands. Moreover, such edge states are topologically protected and can circumvent sharp corners of the domain wall without backscattering, despite the absence of a complete gap in the spectrum of this system. Our results suggest a new platform for observation of the unpaired Dirac cones and open new prospects for investigation of nonlinear effects in topological systems lacking a complete gap.

2. THEORETICAL MODEL

A. Helical Waveguide Array and Its Band Structure

The propagation dynamics of a laser beam in a helical shallow waveguide array can be described by the Schrödinger-like equation for normalized amplitude ψ of the light field:

$$i\frac{\partial\psi}{\partial z} = -\frac{1}{2}\left(\frac{\partial^2}{\partial x^2} + \frac{\partial^2}{\partial y^2}\right)\psi - \mathcal{R}(x, y, z)\psi, \tag{1}$$

where x, y are the transverse coordinates that are to the characteristic scale $r_0 = 10$ μm, z is the propagation distance that is normalized to the diffraction length $kr_0^2 \approx 1.14$ mm, $k = 2\pi n/\lambda$ is the wavenumber in the medium with the background refractive index n (for fused silica $n \approx 1.45$), and $\lambda = 800$ nm is the working wavelength. $\mathcal{R}(x, y, z)$ describes a waveguide array composed from helical Gaussian-shaped waveguides:

$$\mathcal{R} = \sum_{m,n} p_{m,n} \exp\left(-\frac{(x - x_{m,n}(z))^2 + (y - y_{m,n}(z))^2}{d^2}\right). \tag{2}$$

Here, d is the waveguide width, $(x_{m,n}, y_{m,n})$ are the z-dependent coordinates of waveguide centers in the honeycomb grid, $p_{m,n} = k^2 r_0^2 \delta n/n$ is the waveguide depth that is proportional to the refractive index contrast δn in the array (for instance, $p = 1.0$ corresponds to $\delta n \sim 1.1 \times 10^{-4}$), and spacing between neighboring waveguides in the grid is equal to a. In a helical waveguide array, coordinates of waveguides change with z as

$$\begin{cases} x_{m,n}(z) = x_{m,n}(0) + r\sin(\Omega z), \\ y_{m,n}(z) = y_{m,n}(0) + r\cos(\Omega z) - r, \end{cases}$$

where r is the radius of the helix and $\Omega = 2\pi/Z$ is the rotation frequency defined by period Z. We further introduce detuning between two sublattices of the array, by setting depth as $p_{m,n} = p + \delta$ or $p_{m,n} = p - \delta$, where δ is the depth detuning that is connected with different refractive index contrasts in two sublattices and that corresponds to different on-site "energies" in the language of condensed-matter physics [35,38,43], as shown in the schematic array illustration in Fig. 1(a). Further we set the mean waveguide depth $p = 8.9$, typical value of detuning $\delta = 0.1$, waveguide spacing $a = 1.6$ (corresponding to 16 μm), width $d = 0.4$ (corresponding to 4 μm), helix period $Z = 6$ (corresponding to 6.8 mm), and radius $r = 0.4$ (corresponding to 4 μm). These parameters are typical for waveguide arrays inscribed in fused silica using focused pulses from a femtosecond laser [16,44–48].

To analyze the impact of helicity and detuning on band structure, we first consider Floquet-Bloch modes of a bulk array that can be found as $\psi(\boldsymbol{r}, z) = \phi(\boldsymbol{r}, z)\exp(ibz + i\boldsymbol{k}\cdot\boldsymbol{r})$, where the Floquet-Bloch function $\phi(\boldsymbol{r}, z)$ is transverse and Z-periodic, b is the quasi-propagation constant, and $\boldsymbol{k} = (k_x, k_y)$ is the Bloch momentum. The function ϕ and the dependence $b(\boldsymbol{k})$ can be found by solving the equation

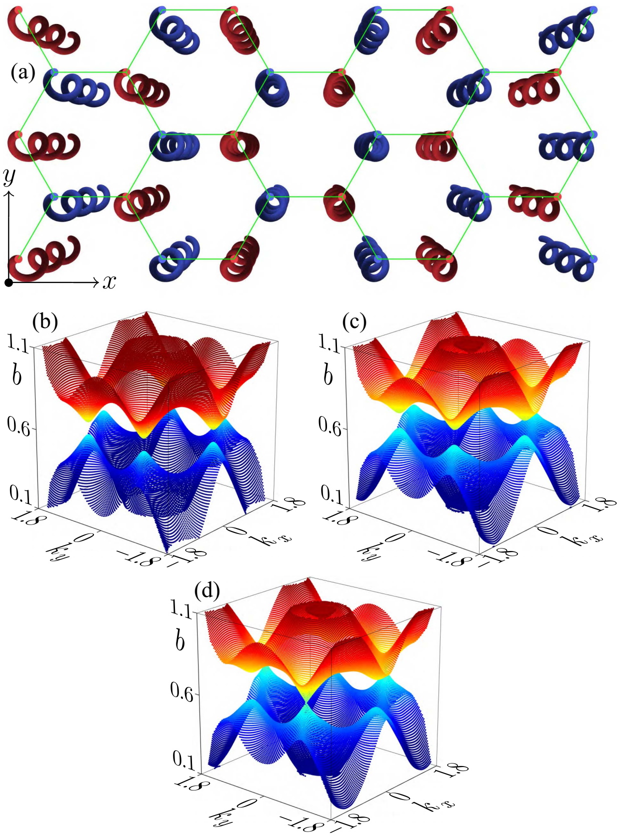

Fig. 1. (a) Schematic illustration of helical waveguide array with detuning between two sublattices, shown with red and blue colors. Green hexagons highlight honeycomb structure of the array. Band structure of bulk waveguide array with (b) $r = 0$ and $\delta = 0.1$, (c) $r = 0.4$ and $\delta = 0$, and (d) $r = 0.4$ and $\delta = 0.1$.

$$b\phi = \frac{1}{2}\left(\frac{\partial^2}{\partial x^2} + \frac{\partial^2}{\partial y^2}\right)\phi + \mathcal{R}(x,y,z)\phi + i\frac{\partial\phi}{\partial z}, \tag{3}$$

using the "propagation and projection" method [27,49,50], which combines plane-wave expansion for calculation of eigenmodes of static arrays and their subsequent propagation in helical structure for calculation of quasi-propagation constants and Floquet-Bloch modes. The spectrum of a static honeycomb array at $\delta, r = 0$ is known to possess six Dirac points, belonging to two groups **K** and **K**′, where top and bottom bands touch. If only the detuning δ is introduced into the structure to break its inversion symmetry, while the waveguides are straight ($r = 0$), all Dirac cones split and become valleys, and a complete gap opens in the spectrum of the system [Fig. 1(b)]. Similar transformation of the spectrum is observed for zero detuning $\delta = 0$, when waveguides are made helical, which leads to the breakup of the time-reversal symmetry of the system [see spectrum in Fig. 1(c)]. It should be stressed, however, that even though Dirac cones split in both Figs. 1(b) and 1(c), the Berry curvature (see definition in Section 2.B) in valleys behaves differently: for the upper band in Fig. 1(c) the curvature becomes positive around all **K** and **K**′ points, while in Fig. 1(b) it acquires opposite signs in **K** and **K**′ points (Berry curvature in the lower band in a given valley is usually opposite to that in the upper band). Therefore, simultaneous breakup of time-reversal symmetry and inversion symmetry in a system with $\delta, r \neq 0$ leads to different variations of Berry curvature in **K** and **K**′ points, which may translate into a competing impact of helicity and detuning on gap width around these points (as originally predicted in the Haldane model [11] for an electronic system). Thus, we find that at $r = 0.4$ the increase of sublattice detuning up to $\delta \approx 0.10$ (for $r_0 = 0.3$ up to $\delta \approx 0.07$) leads to restoration of the Dirac cones in three **K** points, while a gap remains open in three **K**′ points, as shown in Fig. 1(d), i.e., unpaired Dirac cones appear in the bulk spectrum of this system. By changing the sign of detuning δ, one achieves opening of the gap in **K** points instead, while Dirac points are observed in **K**′ points in this case.

Possible scenarios of the band structure transformation are summarized in Table 1, where we use the fact that breakup of the inversion symmetry tends to create valleys, where the Berry curvature in each band is an odd function of $\boldsymbol{k}$, while breakup of time-reversal symmetry tends to create valleys, where the Berry curvature is an even function of $\boldsymbol{k}$ [51]. Thus, when time-reversal and inversion symmetries are broken simultaneously, the total Berry curvature at valleys may be enhanced (gap width increases) or reduced (up to restoration of Dirac point) in comparison with the case when only one of the symmetries is broken. One can therefore distinguish four different situations, highlighted in Table 1, where the symbol X implies the possibility of the Dirac point restoration. For instance, one can see that changing of only rotation direction or inversion of detuning shifts Dirac points from **K** to **K**′ points (or vice versa), while simultaneous change of rotation direction and inversion of detuning will have no effect on the location of the Dirac points. We would like to note that the rotation of the waveguide array in Fig. 1(a) is clockwise ↻, and the results correspond to the case ① in Table 1.

Table 1. Sign of the Berry Curvature $\mathcal{B}$ of Valleys for Different Signs of Detuning and Different Directions of Waveguide Rotation (helicity)[a]

		$\mathcal{B}$(K)	$\mathcal{B}$(K′)
①	$\delta > 0$	–	+
	↻	+	+
	Total	X	+
②	$\delta > 0$	–	+
	↺	–	–
	Total	–	X
③	$\delta < 0$	+	–
	↻	+	+
	Total	+	X
④	$\delta < 0$	+	–
	↺	–	–
	Total	X	–

[a] X means that the Dirac cone may appear. The rotation direction (clockwise ↻ or anti-clockwise ↺) of the waveguide array is defined along negative z-direction (viz., counter to the light propagation direction).

B. Topological Characterization of the System

To characterize topological properties of a helical waveguide array with detuning between two sublattices, we utilize a tight-binding approximation and the approach summarized in Ref. [52]. The evolution of the excitations in our system over one Z-period (in reciprocal space) can be described by the Floquet evolution operator $U(\boldsymbol{k}, Z)$, which allows to formally introduce also the effective Hamiltonian H_{eff}:

$$U(\boldsymbol{k}, Z) = \mathcal{Z}\,\exp\left(-i\int_0^Z H(\boldsymbol{k}, z)\mathrm{d}z\right) = \exp(-iH_{\text{eff}}(\boldsymbol{k})Z), \tag{4}$$

where $\mathcal{Z}$ is the time-ordering operator, and $H(\boldsymbol{k}, z)$ is the "instantaneous" Hamiltonian of the system,

$$H(\boldsymbol{k}, z) = t\begin{bmatrix} \wp & P \\ P^\dagger & -\wp \end{bmatrix}. \tag{5}$$

Here

$$P = \sum_i \exp(-i(\boldsymbol{A} + \boldsymbol{k})\cdot\boldsymbol{e}_i)$$

and

$$\boldsymbol{A}(z) = r\Omega[-\cos(\Omega z), \sin(\Omega z)],$$

where $i = 1, 2, 3$, $\boldsymbol{e}_1 = [1, 0]^{\mathrm{T}}a$, $\boldsymbol{e}_2 = [-1/2, -\sqrt{3}/2]^{\mathrm{T}}a$, $\boldsymbol{e}_3 = [-1/2, \sqrt{3}/2]^{\mathrm{T}}a$ are the characteristic vectors of the honeycomb lattice, $\boldsymbol{A}(z)$ is the gauge field arising due to helicity of waveguides, $\wp$ is the on-site "energy" detuning [53,54] of two sublattices in a tight-binding model, which is different from δ in Eq. (2) but proportional to it, and t is the hopping strength. Berry curvature [42] of the band with index n can be introduced as

$$\mathcal{B}_n(\boldsymbol{k}) = i\sum_{n'\neq n}\left(\frac{\langle u_n|\partial_{k_x}H_{\text{eff}}|u_{n'}\rangle\langle u_{n'}|\partial_{k_y}H_{\text{eff}}|u_n\rangle}{(b_n - b_{n'})^2} - \frac{\langle u_n|\partial_{k_y}H_{\text{eff}}|u_{n'}\rangle\langle u_{n'}|\partial_{k_x}H_{\text{eff}}|u_n\rangle}{(b_n - b_{n'})^2}\right), \tag{6}$$

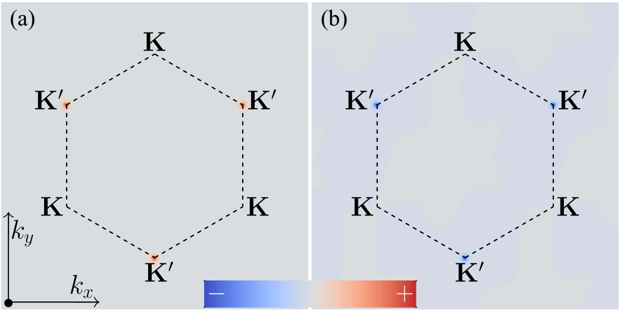

Fig. 2. Berry curvature $\mathcal{B}$ of the bottom band of the lattice with unpaired Dirac cones. Parameters in (a) are: $a = 1.6$, $Z = 6$, $r = 0.3$, $\wp = 0.1$, $t = 0.18$, and $\boldsymbol{A}(z) = r\Omega[-\cos(\Omega z), \sin(\Omega z)]$. Parameters in (b) are: $a = 1.6$, $Z = 6$, $r = 0.3$, $\wp = -0.1$, $t = 0.18$, and $\boldsymbol{A}(z) = r\Omega[-\cos(\Omega z), -\sin(\Omega z)]$. The dashed hexagon represents the first Brillouin zone.

where $|u_n\rangle$ and b are the eigenstates and eigenvalues of H_{eff}, and $\langle\cdot|\cdot\rangle$ is the inner product. Typical distribution $\mathcal{B}_n(\boldsymbol{k})$ in the bottom band ($n = 2$) is presented in Fig. 2(a). It is calculated for a set of parameters $a = 1.6$, $Z = 6$, $r = 0.3$, $\wp = 0.1$, and $t = 0.18$ at which Dirac cones emerge in **K** points, while a gap is opened between **K**′ valleys, where Berry curvature is positive. If one simultaneously changes the sign of detuning $\wp$ and waveguide rotation direction (helicity), the gap again appears between **K**′ valleys, but Berry curvature around them becomes negative in the bottom band, as shown in Fig. 2(b). The topological index characterizing this system is given by the valley Chern number

$$\mathcal{C}_{v,n} = \frac{1}{2\pi}\int_v \mathcal{B}_{v,n}(\boldsymbol{k})\mathrm{d}\boldsymbol{k}, \tag{7}$$

where v indicates that the integration is carried over close proximity of the valleys. Thus, the valley Chern number of each valley in Fig. 2(a) is 1/2 while in Fig. 2(b) it is given by −1/2. Therefore, according to the bulk-edge correspondence principle [7,8], if the interface is created between two such arrays in real space, the difference $1/2 - (-1/2) = 1$ of valley Chern numbers predicts the appearance of the topological edge states connecting the upper and bottom bands around the valley in the band structure. Importantly, this situation sharply contrasts with the usual valley Hall system, where for nonzero detuning $\wp$ the gap simultaneously opens between all valleys in such a way that Berry curvature has opposite signs around **K** and **K**′ valleys, so that the integral Eq. (7) over the entire Brillouin zone yields zero $\mathcal{C}_n$. Instead, in our case such an integral would be nonzero and opposite in sign for both first and second bands.

3. RESULTS AND DISCUSSION

A. Domain Walls and Edge States

To illustrate the possibility of formation of topological edge states in this system with unpaired Dirac points, we constructed the domain wall between helical arrays of types A and B with opposite detuning of two constituent sublattices and with opposite waveguide rotation directions, as illustrated in schematic Figs. 3(a) and 3(b). As discussed previously, the bands of such arrays with the same index n are characterized by the opposite valley Chern numbers, while Dirac cones in both A and B arrays are located in **K** points. The arrays can be arranged either into B-A-B [Fig. 3(a)] or into A-B-A [Fig. 3(b)] configurations, with waveguides of only one type (red or blue) falling onto domain walls; the latter are highlighted by the green dashed lines. Notice that the waveguides on the domain wall have alternative helix directions since they belong to different arrays A and B. According to the bulk-edge correspondence principle the domain walls between such arrays should support edge states of topological origin. In Fig. 3(c) we show the dependence of the quasi-propagation constant of all modes in a B-A-B configuration on Bloch momentum k_y (along the edge) within the first transverse Brillouin zone of width $K = 2\pi/\sqrt{3}a$. Since the array is periodic in z, the spectrum is also periodic along the vertical b axis with the period $\Omega = 2\pi/Z$ (defined by the waveguide rotation frequency). In the band structure in Fig. 3(c) gray dots correspond to delocalized bulk modes, while red and blue dots correspond to the edge states localized on red and blue domain walls, respectively. Upon calculation of this spectrum we "glued" B arrays far away from the domain walls and a wide A layer between them by assuming periodic boundary conditions along the x-axis. The remarkable feature of the "projected" spectrum in Fig. 3(c) is its asymmetry with coexistence of the Dirac cone at $k_y = -K/3$ (indicated by the green arrow) and of a gap at $k_y = +K/3$, around which unidirectional edge states form that are located at blue and red domain walls, in accordance with line colors. The appearance of such edge states is a remarkable fact, taking into account the absence of the complete gap in the spectrum. We show selected profiles of the edge states from red and blue domain walls in Figs. 3(d) and 3(e), respectively. Since our Floquet system is Z-periodic, such states show exactly periodic evolution on one longitudinal period, with substantial variations of the field modulus distribution in the internal z-points. Notice that localization of such edge states is strongest in the center of the "local" gap, while when their quasi-propagation constant approaches the band, such states gradually become extended.

The edge states reported here require for their existence the interface between two lattices with broken inversion symmetry and for this reason they do belong to the class of valley Hall states. However, our structure also combines in a unique fashion the properties typical for valley Hall and Floquet systems. Because time-reversal symmetry in our system is broken due to the helicity of waveguides, edge states become truly unidirectional and this allows to avoid the problem typical for usual valley Hall systems that support a pair of counterpropagating edge states that can be coupled by sufficiently narrow edge defects. Our system is free from this limitation and this is reflected in a completely different scenario of interaction of edge states with narrow defects that is now accompanied not by reflection of the edge state, but by emission of fraction of power in the form of a conical wave (please see Fig. 6) and passage of a considerable fraction of power through the defect. In this sense, our system offers stronger topological protection than conventional valley Hall systems.

B. Topological Protection of the Edge States

To confirm the topological nature of the Floquet edge states suggested by associated nonzero valley Chern numbers discussed in Section 2.B, we designed two types of the domain walls with a zigzag shape that possess two sharp corners (the

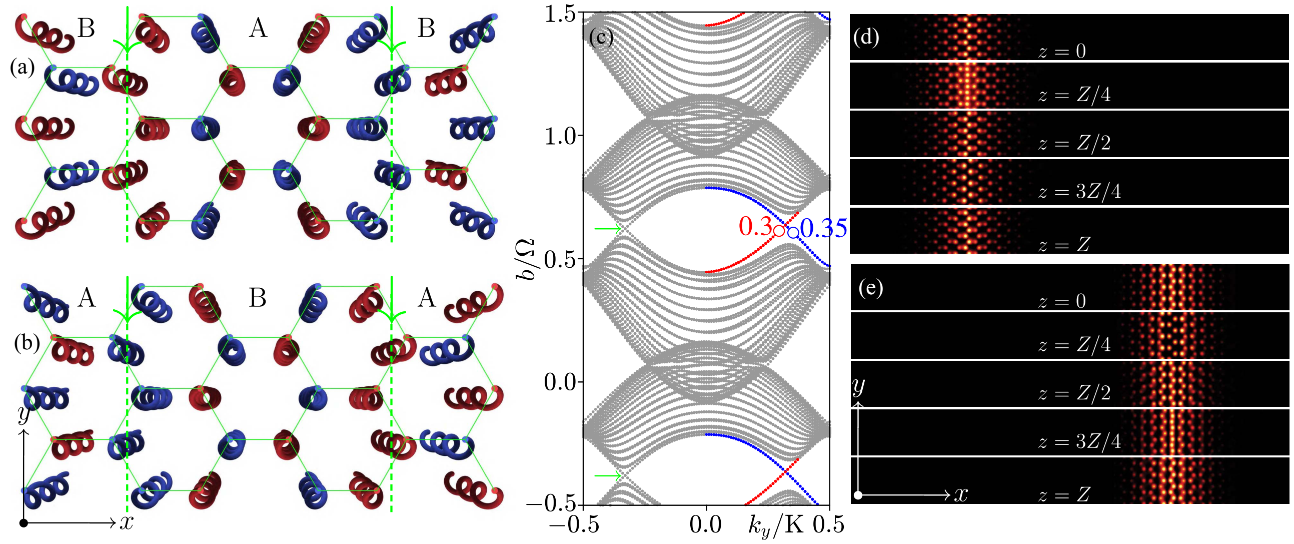

Fig. 3. (a) Schematic representation of composite helical waveguide array with two domain walls that are indicated by the vertical dashed green lines. Only waveguides of one type (blue or red) fall onto domain wall. The array is periodic in the y direction. Both detuning and direction of waveguide rotation are opposite in A and B arrays forming the domain wall. (b) A-B-A array configuration with two domain walls. (c) Quasi-propagation constant versus Bloch momentum k_y for B-A-B configuration in (a). Two longitudinal Brillouin zones are shown to stress vertical periodicity of the spectrum. Red and blue dots correspond to the edge states appearing on red and blue domain walls, respectively. Gray dots correspond to bulk modes. (d) Field modulus distribution $|\psi|$ of the edge state (three y-periods are shown) with $k_y/K=0.3$ residing on the red domain wall in (c) at different propagation distances within one period Z. (e) Edge states with $k_y/K=0.35$ from blue domain wall at different distances. In all cases $Z=6$, $r_0=0.3$, and $\delta=0.07$.

angle is 60°). The domain wall in Fig. 4(a) is similar to the red domain wall in Fig. 3(a), as highlighted by the corresponding line, while the domain wall in Fig. 4(b) is similar to the blue domain wall in Fig. 3(a), and is highlighted by the blue line. These domain walls support edge states corresponding to red and blue branches of Fig. 3(c) that have opposite group

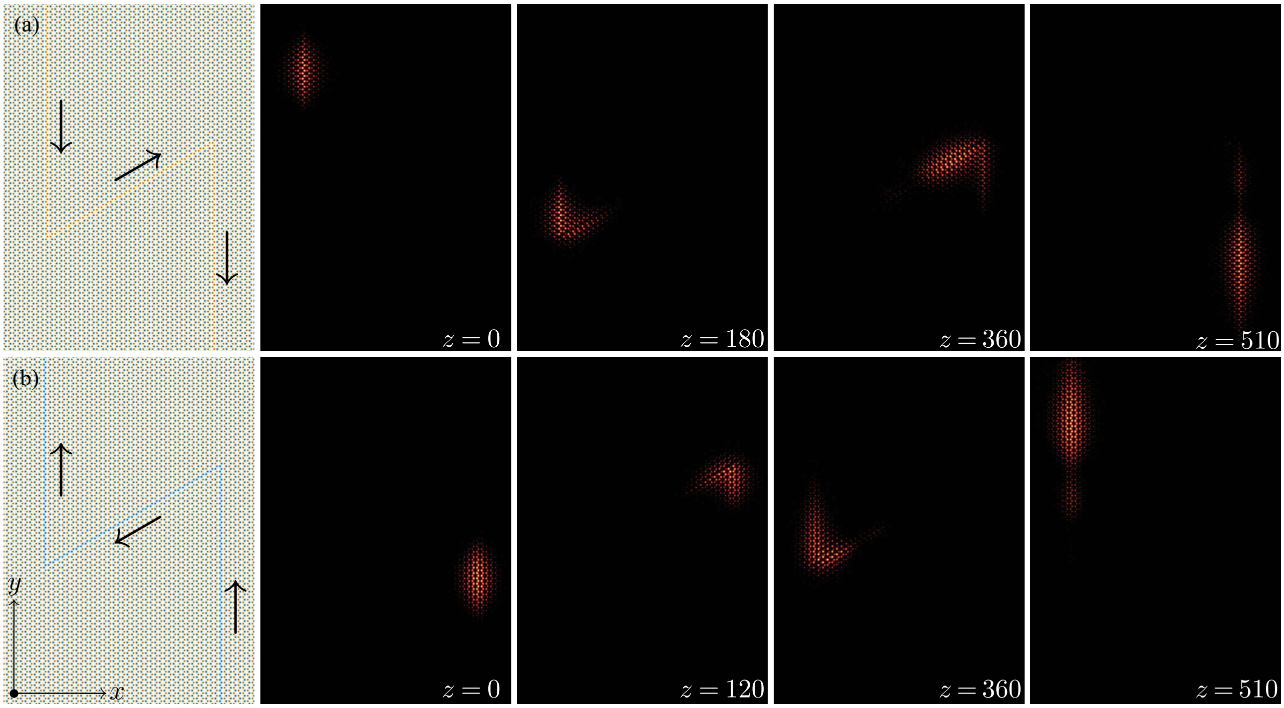

Fig. 4. Zigzag-shaped domain walls with sharp corners that are adopted for demonstration of the topological protection of the edge states from the (a) red branch and (b) blue branch of Fig. 3(c). The arrows indicate the direction of motion of the edge states with initial broad envelope at different stages of propagation. Corresponding field modulus distributions at different distances are shown too. The two edge states correspond to $k_y/K=0.3$ (a) and $k_y/K=0.35$ (b).

velocities $v_g = -b' = -\mathrm{d}b/\mathrm{d}k_y$. Since $b' > 0$ for the red edge state (see red curve in Fig. 5), it moves in the negative y-direction, while its blue counterpart with $b' < 0$ moves in the positive direction of the y-axis (see blue curve in Fig. 5). The propagation dynamics of corresponding edge states with initial broad envelopes is illustrated in Figs. 4(a) and 4(b); the direction of motion of corresponding states is highlighted by the black arrows on schematics with zigzag domain walls. Field modulus distributions at different distances clearly show that both red and blue edge states can circumvent sharp corners during propagation without any noticeable backscattering, which illustrates their topological protection, at least for such types of edge deformations. Notice that small tails visible in field modulus distributions at $z = 510$ are due to dispersion of the wavepacket, as they move in the same direction as the wavepacket and with the same velocity. This is an intriguing result, taking into account the absence of a complete gap in the spectrum of the system. We would like to note that in the dynamics illustrated in Fig. 4 the edge state shows neither inter-valley scattering nor excitation of bulk states because this state is taken quite close to the $\mathbf{K}'$ point in momentum space, and its quasi-propagation constant is located practically in the center of the gap. However, if the input edge state is taken further from the $\mathbf{K}'$ point, for example, with $k_y = 0.2K$, such that its quasi-propagation constant can overlap with quasi-propagation constants of the bulk modes, a fraction of power can be radiated into the bulk when the state bypasses the sharp corner (see Appendix A for corresponding results).

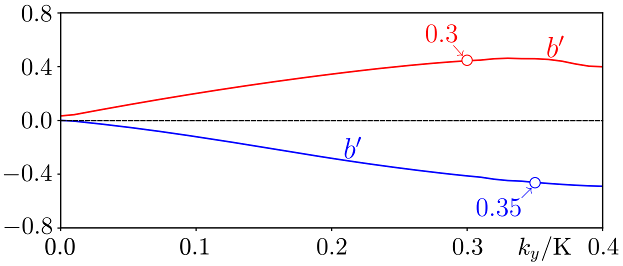

Fig. 5. First-order derivative b' of the quasi-propagation constant of the valley Hall edge states at $Z = 6$ and $r_0 = 0.3$.

It is a well-established fact that in valley Hall systems the inter-valley scattering can be induced by strongly localized defects, while broad, slowly changing defects cannot induce such scattering. To test the behavior of the edge states in our system with respect to strongly localized perturbations, we removed one waveguide located on the domain wall, as illustrated by the green circle in Fig. 6. The incident edge state at $z = 0$ in Fig. 6(b) is the same as in Fig. 4(a) and it encounters the defect around $z = 110$ [Fig. 6(c)] while propagating along the domain wall. The interaction between the defect and the edge state shows that the edge state cannot bypass the defect without radiation [see Figs. 6(d) and 6(e)]. Remarkably, because edge states in our system are unidirectional, no backward reflection at the defect occurs. Instead, inter-valley scattering leads to the excitation of waves in close proximity of the Dirac cone at the $\mathbf{K}$ point, and further propagation of such waves is accompanied by their conical diffraction resulting in a gradually expanding ring visible in field modulus distributions at $z = 230$ and $z = 300$. The dashed cyan circle in Figs. 6(d) and 6(e) [and also in Fig. 6(h)] illustrates the theoretically evaluated radius of the conical diffraction pattern $\sim|b'_{\mathbf{K}}(z - 110)|$, with $b'_{\mathbf{K}} \sim 0.45$ being the first-order derivative of the quasi-propagation constant around the Dirac cone at the $\mathbf{K}$ point. Remarkably, only a fraction of input power is emitted in the form of a conical wave after the interaction width defect, while the rest of the

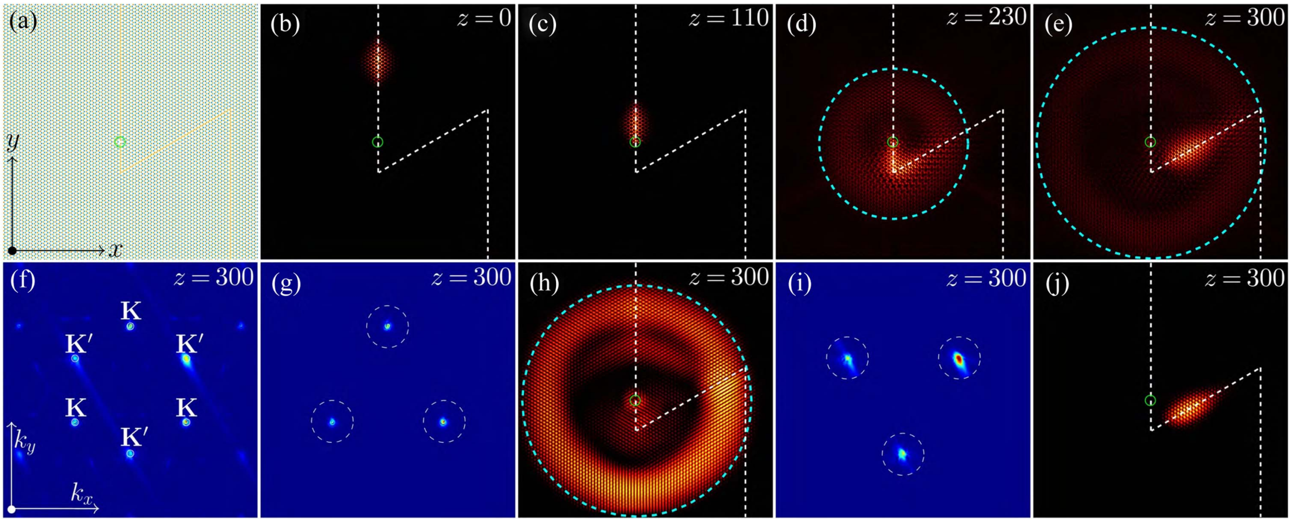

Fig. 6. (a) A zigzag domain wall with a defect in the form of missing waveguide indicated by the green circle. (b)–(e) Spatial field modulus distributions in the edge state at different propagation distances. Cyan dashed circle highlights theoretical radius of the conical diffraction pattern. (f) Total spatial spectrum of the edge state at $z = 300$. (g) Part of the spectrum at $z = 300$ where only contribution from regions around $\mathbf{K}$ points is left (see white dashed circles), while spectral intensity around $\mathbf{K}'$ points is set to zero. (h) Field modulus distribution in the form of conical wave produced by spectrum in (g). (i) Part of the spectrum at $z = 300$ where only contribution from regions around $\mathbf{K}'$ points is left (see dashed circles), while spectral intensity around $\mathbf{K}$ points is set to zero. (j) Field modulus distribution of the edge state produced by spectrum in (i). White dashed line represents the zigzag domain wall. The parameters are the same as in Fig. 4.

power is organized into an edge state that bypasses the defect and keeps moving along the domain wall—a consequence of the unidirectional nature of the edge states in our system. To illustrate this, we take the exemplary field distribution at $z = 300$ and display its total spatial spectrum in Fig. 6(f). Clearly, there is light around both $\mathbf{K}$ and $\mathbf{K}'$ points. If we isolate contributions from $\mathbf{K}$ points by applying the filter of the form

$$F_{\mathbf{K}}(\boldsymbol{k}) = \begin{cases} 1, |\boldsymbol{k} - \mathbf{K}| \le r_k, \\ 0, \text{other places}, \end{cases} \tag{8}$$

to the total spectrum, where $r_k = 4\sqrt{3}\pi/27a$ is the radius of the circular filter, we will obtain the spectrum depicted in Fig. 6(g) (white dashed circles show the regions outside where the spectral intensity was set to zero), which corresponds to the field distribution shown in Fig. 6(h) in the form of a clear conical diffraction pattern. In contrast, if the filter $F_{\mathbf{K}'}(\boldsymbol{k})$ is applied that isolates contributions from $\mathbf{K}'$ points [see the resulting spectrum in Fig. 6(i)], in the spatial domain one obtains the spatial distribution depicted in Fig. 6(j), which clearly shows that the edge state partially bypasses the defect and keeps propagating along the domain wall after emission of a fraction of its initial power in the form of a conical wave. Because the edge states reported here bypass strongly localized defects with emission of a fraction of power in the form of conical waves, at the same time they can still clearly bypass sharp corners practically without radiation, akin to edge states in valley Hall systems reported previously [38,39]; we attribute them to this last class of edge states.

C. Excitation of the Valley Hall Edge States

We would like to note that the valley Hall edge states reported here can be efficiently excited by a Gaussian beam with proper initial tilt (i.e., we multiply the input field distribution with $e^{ik_x x + ik_y y}$ term). In Fig. 7, we display an example of such excitation dynamics. The elliptical Gaussian beam is launched at the left branch of the zigzag domain wall [see field modulus distribution in Fig. 7(a) and corresponding spatial spectrum in Fig. 7(b)]. This input beam quickly reshapes and after emission of some radiation efficiently excites the moving valley Hall edge state with Bloch momentum k_y corresponding to the initial momentum of the Gaussian beam. The excited moving edge state bypasses the zigzag bend of the domain wall without reflections. The spectra at different distances presented in Fig. 7(b) demonstrate that the beam is always concentrated around the $\mathbf{K}'$ points. The efficiency of this excitation process strongly depends on the momentum of the initial Gaussian beam. For example, if its spectrum of the input beam is shifted away from $\mathbf{K}'$ valleys, one observes considerable diffractive broadening in real space without obvious excitation of localized edge states. For instance, if the input beam excites the $\mathbf{K}$ valley for a given type of the domain wall, one observes conical diffraction in the spatial domain [2].

4. CONCLUSION AND OUTLOOK

In summary, we have shown that helical waveguide arrays with detuning between two sublattices, where time-reversal and inversion symmetries are simultaneously broken, can feature unpaired Dirac points in their linear spectra. The formation of the unpaired Dirac points in $\mathbf{K}$ or $\mathbf{K}'$ points of the Brillouin zone can be controlled by the sign of detuning and waveguide helicity. Even though the location of Dirac cones does not change upon simultaneous change of the sign of detuning and waveguide helicity, the sign of Berry curvature

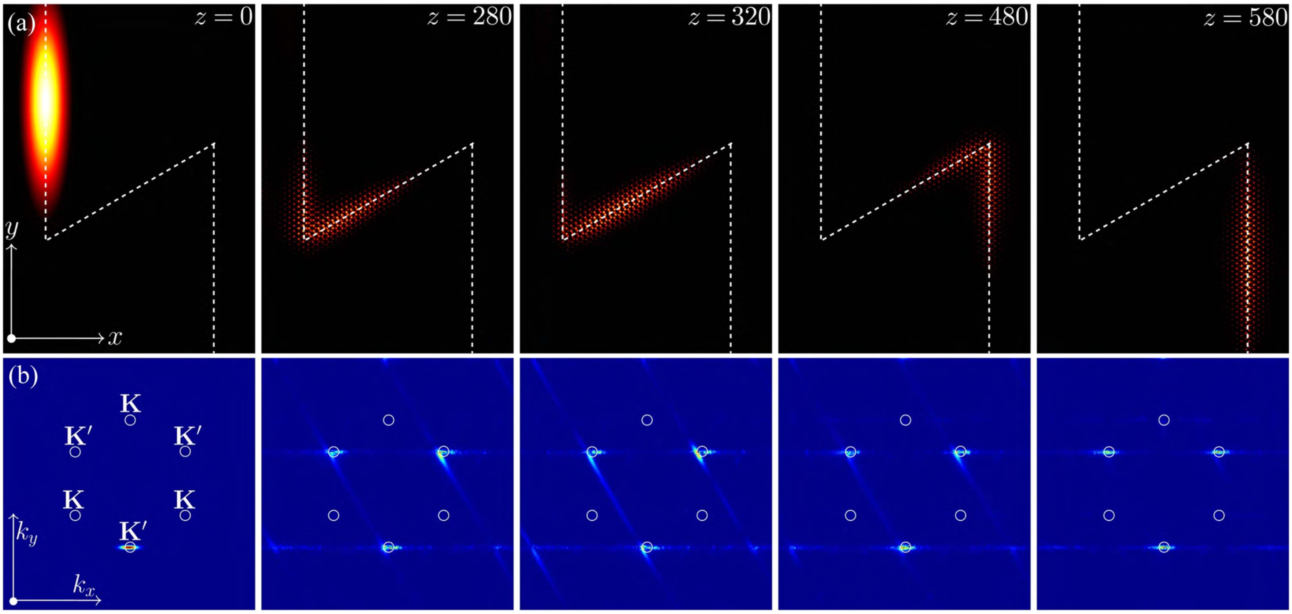

Fig. 7. Dynamics of excitation of the valley Hall edge state with a tilted elliptical Gaussian beam. (a) Input field modulus distribution at $z = 0$ and field modulus distributions at progressively increasing propagation distances, indicating that the excited state bypasses zigzag bend of the domain wall, indicated with white dashed line. (b) Spectra in momentum space corresponding to spatial distributions in (a). Circles in (b) highlight the valleys in six corners of the first Brillouin zone. Parameters of the array are the same as in Fig. 4. The input Gaussian beam has width $w_x = 10$, $w_y = 20\sqrt{5}$ and initial momentum $k_x = 0$, $k_y = -4\pi/3\sqrt{3}a$.

changes, which allows to construct the interface between two arrays with opposite valley Chern numbers, hosting unidirectional topological edge states. These states are topologically protected despite the absence of the complete gap in the spectrum of the system. These results suggest a platform and pave the way to exploration of various nonlinear phenomena in Floquet insulators with unpaired Dirac points. For instance, we would like to point out that in the past decade a variety of hybrid topological edge solitons have been reported in topological systems based on helical waveguide arrays [17,18,55–60], in valley Hall arrays with straight waveguides [37–41,61,62], and other systems [14,63–66], but all these structures are characterized by the presence of complete topological gaps and, as a rule, are developed on lattices possessing paired Dirac points. Similarly, generation of higher harmonics and topological lasers may acquire very unusual features in systems with unpaired Dirac points. Last but not least, the unpaired Dirac cones ensure that the inter-valley scattering will not happen in the system developed in the work, which may bring a different view on the conclusions reported very recently [67,68]. We believe that the system with unpaired Dirac cones may provide a novel platform for investigating higher-order topological states [69–71] and may help to observe the unpaired Weyl points [72].

APPENDIX A

The edge states with $k_y = 0.30K$ and $k_y = 0.35K$, whose propagation dynamics is shown in Fig. 4 in the main text, are taken sufficiently close to the $\mathbf{K}'$ point, so that their quasi-propagation constants are located nearly in the center of the local gap [see Fig. 3(c) in the main text]. Edge states, however, exist in a sufficiently broad interval of k_y values, so the natural question arises how they interact with sharp bends of the domain wall. To answer this question, we consider here the dynamics of propagation at zigzag domain wall of the edge state with $k_y = 0.20K$, taken further away from the $\mathbf{K}'$ point—see field modulus distributions at different distances in Fig. 8(a), and corresponding spatial spectra in Fig. 8(b). Other parameters are the same as for Fig. 4(a) in the main text. The peculiarity of this edge state is that its quasi-propagation constant overlaps with quasi-propagation constants of bulk modes in the vicinity of the $\mathbf{K}'$ point. Due to this, a fraction of the input power can be radiated into the bulk, as one clearly sees from distributions at $z = 330$, when the edge state bypasses sharp bends of the domain wall. Remarkably, the edge state still does not exhibit backward reflection [see also the spectrum in Fig. 8(b), where spectral intensity remains negligible around all $\mathbf{K}$ points]. After emission of radiation, the edge state keeps propagating along the domain wall, as one can see from the distribution at $z = 390$. Notice that when k_y value is selected such that quasi-propagation constant of the edge state does not overlap with b of the bulk modes, this radiation vanishes.

Funding. Natural Science Basic Research Program of Shaanxi Province (2024JC-JCQN-06); National Natural Science Foundation of China (12074308, 12304370); Fundamental Research Funds for the Central Universities (sxzy012024146); Research Project of the Institute of Spectroscopy of the Russian Academy of Sciences (FFUU-2024-0003).

Acknowledgment. The authors appreciate the three anonymous reviewers for their insightful and helpful comments that improved the work greatly.

Disclosures. The authors declare no conflicts of interest.

Data Availability. Data underlying the results presented in this paper are not publicly available at this time but may be obtained from the authors upon reasonable request.

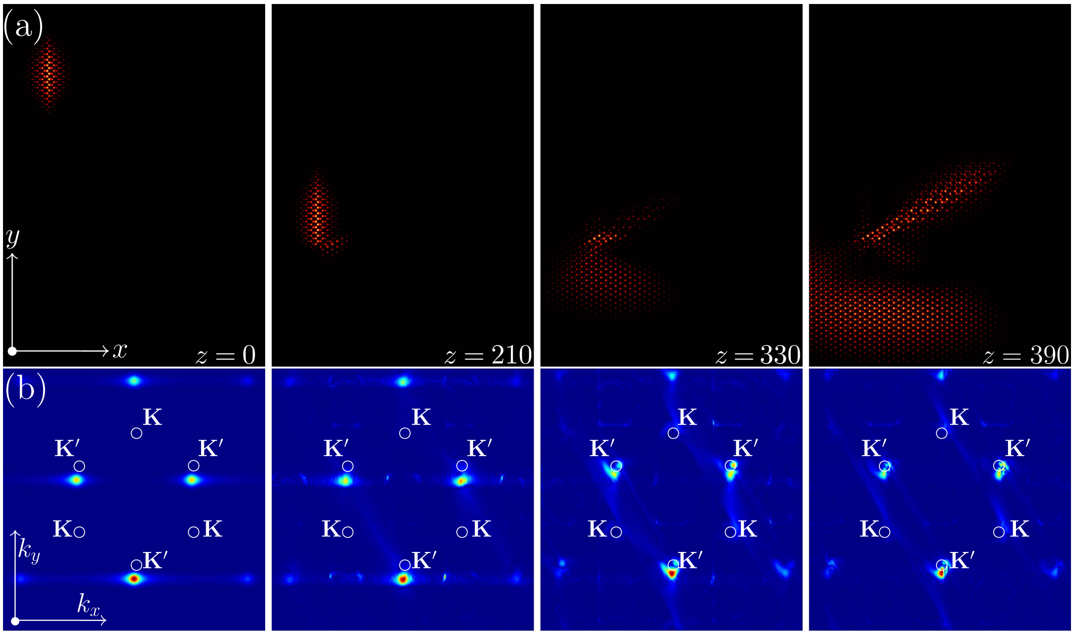

Fig. 8. Setup similar to that of Fig. 4(a), but for the edge state with $k_y = 0.2K$.

REFERENCES

1. D. Leykam and A. S. Desyatnikov, “Conical intersections for light and matter waves,” Adv. Phys. X **1**, 101–113 (2016).
2. O. Peleg, G. Bartal, B. Freedman, *et al.*, “Conical diffraction and gap solitons in honeycomb photonic lattices,” Phys. Rev. Lett. **98**, 103901 (2007).
3. D. Song, V. Paltoglou, S. Liu, *et al.*, “Unveiling pseudospin and angular momentum in photonic grapheme,” Nat. Commun. **6**, 6272 (2015).
4. Z. Y. Zhang, R. Wang, Y. Q. Zhang, *et al.*, “Observation of edge solitons in photonic graphene,” Nat. Commun. **11**, 1902 (2020).
5. W. Yan, H. Zhong, D. Song, *et al.*, “Flatband line states in photonic super-honeycomb lattices,” Adv. Opt. Mater. **8**, 1902174 (2020).
6. A. H. C. Neto, F. Guinea, N. M. R. Peres, *et al.*, “The electronic properties of graphene,” Rev. Mod. Phys. **81**, 109–162 (2009).
7. L. Lu, J. D. Joannopoulos, and M. Soljačić, “Topological photonics,” Nat. Photonics **8**, 821–829 (2014).
8. T. Ozawa, H. M. Price, A. Amo, *et al.*, “Topological photonics,” Rev. Mod. Phys. **91**, 015006 (2019).
9. D. Smirnova, D. Leykam, Y. Chong, *et al.*, “Nonlinear topological photonics,” Appl. Phys. Rev. **7**, 021306 (2020).
10. Q. Yan, X. Hu, Y. Fu, *et al.*, “Quantum topological photonics,” Adv. Opt. Mater. **9**, 2001739 (2021).
11. F. D. M. Haldane, “Model for a quantum Hall effect without Landau levels: condensed-matter realization of the ‘parity anomaly’,” Phys. Rev. Lett. **61**, 2015–2018 (1988).
12. Z. Wang, Y. Chong, J. D. Joannopoulos, *et al.*, “Observation of unidirectional backscattering-immune topological electromagnetic states,” Nature **461**, 772–775 (2009).
13. A. V. Nalitov, D. D. Solnyshkov, and G. Malpuech, “Polariton *Z* topological insulator,” Phys. Rev. Lett. **114**, 116401 (2015).
14. Y. V. Kartashov and D. V. Skryabin, “Modulational instability and solitary waves in polariton topological insulators,” Optica **3**, 1228–1236 (2016).
15. S. Klembt, T. H. Harder, O. A. Egorov, *et al.*, “Exciton-polariton topological insulator,” Nature **562**, 552–556 (2018).
16. M. C. Rechtsman, J. M. Zeuner, Y. Plotnik, *et al.*, “Photonic Floquet topological insulators,” Nature **496**, 196–200 (2013).
17. Y. Lumer, Y. Plotnik, M. C. Rechtsman, *et al.*, “Self-localized states in photonic topological insulators,” Phys. Rev. Lett. **111**, 243905 (2013).
18. M. J. Ablowitz and J. T. Cole, “Tight-binding methods for general longitudinally driven photonic lattices: edge states and solitons,” Phys. Rev. A **96**, 043868 (2017).
19. S. Stützer, Y. Plotnik, Y. Lumer, *et al.*, “Photonic topological Anderson insulators,” Nature **560**, 461–465 (2018).
20. E. Lustig, S. Weimann, Y. Plotnik, *et al.*, “Photonic topological insulator in synthetic dimensions,” Nature **567**, 356–360 (2019).
21. M. S. Rudner, N. H. Lindner, E. Berg, *et al.*, “Anomalous edge states and the bulk-edge correspondence for periodically driven two-dimensional systems,” Phys. Rev. X **3**, 031005 (2013).
22. M. S. Rudner and N. H. Lindner, “Band structure engineering and non-equilibrium dynamics in Floquet topological insulators,” Nat. Rev. Phys. **2**, 229–244 (2020).
23. S. Yin, E. Galiffi, and A. Alù, “Floquet metamaterials,” eLight **2**, 8 (2022).
24. W. Song, H. Li, S. Gao, *et al.*, “Subwavelength self-imaging in cascaded waveguide arrays,” Adv. Photon. **2**, 036001 (2020).
25. B.-C. Xu, B.-Y. Xie, L.-H. Xu, *et al.*, “Topological Landau-Zener nanophotonic circuits,” Adv. Photon. **5**, 036005 (2023).
26. Z. Zhang, Y. Li, X. Sun, *et al.*, “Visual observation of photonic Floquet-Bloch oscillations,” Light Sci. Appl. **13**, 99 (2024).
27. D. Leykam, M. C. Rechtsman, and Y. D. Chong, “Anomalous topological phases and unpaired Dirac cones in photonic Floquet topological insulators,” Phys. Rev. Lett. **117**, 013902 (2016).
28. J. Noh, S. Huang, D. Leykam, *et al.*, “Experimental observation of optical Weyl points and Fermi arc-like surface states,” Nat. Phys. **13**, 611–617 (2017).
29. G. Q. Liang and Y. D. Chong, “Optical resonator analog of a two-dimensional topological insulator,” Phys. Rev. Lett. **110**, 203904 (2013).
30. M. Pasek and Y. D. Chong, “Network models of photonic Floquet topological insulators,” Phys. Rev. B **89**, 075113 (2014).
31. Y. D. Chong and M. C. Rechtsman, “Tachyonic dispersion in coherent networks,” J. Opt. **18**, 014001 (2016).
32. G.-G. Liu, P. Zhou, Y. Yang, *et al.*, “Observation of an unpaired photonic Dirac point,” Nat. Commun. **11**, 1873 (2020).
33. H. Wang, B. Xie, and W. Ren, “Coexistence of chiral and antichiral edge states in photonic crystals,” Laser Photon. Rev. **18**, 2300764 (2024).
34. Y. Wang, H.-X. Wang, L. Liang, *et al.*, “Hybrid topological photonic crystals,” Nat. Commun. **14**, 4457 (2023).
35. J. Noh, S. Huang, K. P. Chen, *et al.*, “Observation of photonic topological valley Hall edge states,” Phys. Rev. Lett. **120**, 063902 (2018).
36. X. Wu, Y. Meng, J. Tian, *et al.*, “Direct observation of valley-polarized topological edge states in designer surface plasmon crystals,” Nat. Commun. **8**, 1304 (2017).
37. H. Zhong, S. Xia, Y. Zhang, *et al.*, “Nonlinear topological valley Hall edge states arising from type-II Dirac cones,” Adv. Photon. **3**, 056001 (2021).
38. Q. Tang, B. Ren, V. O. Kompanets, *et al.*, “Valley Hall edge solitons in a photonic graphene,” Opt. Express **29**, 39755–39765 (2021).
39. B. Ren, H. Wang, V. O. Kompanets, *et al.*, “Dark topological valley Hall edge solitons,” Nanophotonics **10**, 3559–3566 (2021).
40. Y. Tian, Y. Zhang, Y. Li, *et al.*, “Vector valley Hall edge solitons in the photonic lattice with type-II Dirac cones,” Front. Phys. **17**, 53503 (2022).
41. Q. Tang, Y. Zhang, Y. V. Kartashov, *et al.*, “Vector valley Hall edge solitons in superhoneycomb lattices,” Chaos Solitons Fractals **161**, 112364 (2022).
42. D. Xiao, M.-C. Chang, and Q. Niu, “Berry phase effects on electronic properties,” Rev. Mod. Phys. **82**, 1959–2007 (2010).
43. H. Zhong, Y. Q. Zhang, Y. Zhu, *et al.*, “Transport properties in the photonic super-honeycomb lattice—a hybrid fermionic and bosonic system,” Ann. Phys. **529**, 1600258 (2017).
44. M. S. Kirsch, Y. Zhang, M. Kremer, *et al.*, “Nonlinear second-order photonic topological insulators,” Nat. Phys. **17**, 995–1000 (2021).
45. B. Ren, A. A. Arkhipova, Y. Zhang, *et al.*, “Observation of nonlinear disclination states,” Light Sci. Appl. **12**, 194 (2023).
46. A. A. Arkhipova, Y. Zhang, Y. V. Kartashov, *et al.*, “Observation of π solitons in oscillating waveguide arrays,” Sci. Bull. **68**, 2017–2024 (2023).
47. D. Tan, Z. Wang, B. Xu, *et al.*, “Photonic circuits written by femtosecond laser in glass: improved fabrication and recent progress in photonic devices,” Adv. Photon. **3**, 024002 (2021).
48. L. Li, W. Kong, and F. Chen, “Femtosecond laser-inscribed optical waveguides in dielectric crystals: a concise review and recent advances,” Adv. Photon. **4**, 024002 (2022).
49. B. Ren, Y. V. Kartashov, H. Wang, *et al.*, “Floquet topological insulators with hybrid edges,” Chaos Solitons Fractals **166**, 113010 (2023).
50. S. Shen, Y. V. Kartashov, Y. Li, *et al.*, “Floquet edge solitons in modulated trimer waveguide arrays,” Phys. Rev. Appl. **20**, 014012 (2023).
51. S. Raghu and F. D. M. Haldane, “Analogs of quantum-Hall-effect edge states in photonic crystals,” Phys. Rev. A **78**, 033834 (2008).
52. H. Zhong, D. Mihalache, S. Shen, *et al.*, “The band structure of helical waveguide arrays in topological photonics: a tutorial,” Rom. Rep. Phys. **76**, 903 (2024).
53. D. Xiao, W. Yao, and Q. Niu, “Valley-contrasting physics in graphene: magnetic moment and topological transport,” Phys. Rev. Lett. **99**, 236809 (2007).
54. H. Xue, Y. Yang, and B. Zhang, “Topological valley photonics: physics and device applications,” Adv. Photon. Res. **2**, 2100013 (2021).
55. S. K. Ivanov, Y. V. Kartashov, A. Szameit, *et al.*, “Vector topological edge solitons in Floquet insulators,” ACS Photon. **7**, 735–745 (2020).
56. S. K. Ivanov, Y. V. Kartashov, L. J. Maczewsky, *et al.*, “Edge solitons in Lieb topological Floquet insulator,” Opt. Lett. **45**, 1459–1462 (2020).

57. S. K. Ivanov, Y. V. Kartashov, L. J. Maczewsky, *et al.*, "Bragg solitons in topological Floquet insulators," Opt. Lett. **45**, 2271–2274 (2020).
58. S. K. Ivanov, Y. V. Kartashov, M. Heinrich, *et al.*, "Topological dipole Floquet solitons," Phys. Rev. A **103**, 053507 (2021).
59. S. K. Ivanov, Y. V. Kartashov, A. Szameit, *et al.*, "Floquet edge multicolor solitons," Laser Photon. Rev. **16**, 2100398 (2022).
60. S. Mukherjee and M. C. Rechtsman, "Observation of Floquet solitons in a topological bandgap," Science **368**, 856–859 (2020).
61. D. A. Smirnova, L. A. Smirnov, D. Leykam, *et al.*, "Topological edge states and gap solitons in the nonlinear Dirac model," Laser Photon. Rev. **13**, 1900223 (2019).
62. Q. Tang, B. Ren, M. R. Belić, *et al.*, "Valley Hall edge solitons in the Kagome photonic lattice," Rom. Rep. Phys. **74**, 504 (2022).
63. D. R. Gulevich, D. Yudin, D. V. Skryabin, *et al.*, "Exploring nonlinear topological states of matter with exciton-polaritons: edge solitons in Kagome lattice," Sci. Rep. **7**, 1780 (2017).
64. C. Li, F. Ye, X. Chen, *et al.*, "Lieb polariton topological insulators," Phys. Rev. B **97**, 081103 (2018).
65. Y. Q. Zhang, Y. V. Kartashov, and A. Ferrando, "Interface states in polariton topological insulators," Phys. Rev. A **99**, 053836 (2019).
66. W. Zhang, X. Chen, Y. V. Kartashov, *et al.*, "Coupling of edge states and topological Bragg solitons," Phys. Rev. Lett. **123**, 254103 (2019).
67. C. A. Rosiek, G. Arregui, A. Vladimirova, *et al.*, "Observation of strong backscattering in valley-Hall photonic topological interface modes," Nat. Photonics **17**, 386–392 (2023).
68. M. C. Rechtsman, "Reciprocal topological photonic crystals allow backscattering," Nat. Photonics **17**, 383–384 (2023).
69. B. Xie, H.-X. Wang, X. Zhang, *et al.*, "Higher-order band topology," Nat. Rev. Phys. **3**, 520–532 (2021).
70. Z.-K. Lin, Q. Wang, Y. Liu, *et al.*, "Topological phenomena at defects in acoustic, photonic and solid-state lattices," Nat. Rev. Phys. **5**, 483–495 (2023).
71. Y. Zhang, D. Bongiovanni, Z. Wang, *et al.*, "Realization of photonic p-orbital higher-order topological insulators," eLight **3**, 5 (2023).
72. C. Guo, V. S. Asadchy, B. Zhao, *et al.*, "Light control with Weyl semimetals," eLight **3**, 2 (2023).